Materials Advances

ROYAL SOCIETY OF CHEMISTRY

PAPER

View Article Online
View Journal | View Issue

Cite this: *Mater. Adv.*, 2025, 6, 8602

2D-Germanane-reinforced poly(lactic acid): nanocomposites with enhanced antioxidative and antibacterial activity

Theodosis Giousis, †[ab] Zoi Terzopoulou, *[c] Maria-Eirini Grigora, [d] Dimitrios Moschovas, [b] Stamatia Spyrou, [e] Renia Fotiadou, ‡[e] Haralambos Stamatis, [e] Apostolos Avgeropoulos, [b] Dimitrios Tzetzis, [d] Dimitrios P. Gournis, [bf] Dimitrios N. Bikiaris [g] and Petra Rudolf *[a]

Poly(lactic acid) (PLA) is a widely used biobased polymer, but its slow crystallization, brittleness, and limited functional properties restrict broader applications. In this study, we report the first incorporation of germanane (GeH) into PLA *via* solution mixing to produce nanocomposites. Adequate dispersion was achieved at low GeH loadings (0.5–3.0 wt%), while higher concentrations (5.0 wt%) led to aggregation. The addition of small amounts of GeH significantly accelerated PLA crystallization and enhanced local mechanical properties, although thermal stability was slightly reduced. Notably, the nanocomposites exhibited antioxidative and antibacterial activities, arising from the intrinsic properties of GeH. These findings highlight that very low GeH loadings are sufficient to enhance both structural and functional performance. The combination of improved crystallization, mechanical behavior, and bioactive properties positions PLA/GeH nanocomposites as promising candidates for applications in bioactive packaging and biomedical materials.

Received 25th June 2025,
Accepted 10th October 2025

DOI: 10.1039/d5ma00676g

rsc.li/materials-advances

1. Introduction

Poly(lactic acid) (PLA) is undeniably the most popular biobased polymer for both short and long term applications,[1,2] ranging from single-use plastics to biomedical applications to 3D printing.[3,4] While PLA offers compostability and relatively high stiffness, it suffers from brittleness, low impact strength, and slow crystallization. To overcome these limitations, PLA has been combined with various nanofillers, including 2D materials such as clays and graphene, which have been shown to enhance thermal, mechanical, electrical, and crystallization properties, as well as biocompatibility.[5–12]

Following the success of graphene, attention has turned to other 2D monoelemental Xenes, such as phosphorene, antimonene, silicene, and germanene. Germanane (GeH), which is used in this study, is the hydrogenated counterpart of germanene and possesses several distinctive advantages over conventional 2D fillers. Its hydrogen-terminated surface enables facile functionalization for strong interfacial adhesion with PLA without harsh treatments. Unlike defect-rich graphene oxide or metallic MXenes, GeH exhibits a direct bandgap (~1.6 eV) and high carrier mobility, which allow visible-light activity, reactive oxygen species generation, and simultaneous antioxidant and antibacterial effects. Its nonmetallic composition reduces cytotoxicity risks, and it can be dispersed under mild conditions while preserving PLA's transparency and minimizing embrittlement at low loadings.[13,14]

Germanane was first synthesized *via* topochemical reaction of $CaGe_2$ with HCl at low temperature.[15,16] Earlier methods were time-consuming, and produced material with limited thermal stability and purity. Our previously developed synthetic protocol yields highly pure, thermally stable GeH in minutes,[17] which is critical for high-performance PLA nanocomposites.

[a] *Zernike Institute for Advanced Materials, University of Groningen, Nijenborgh 3, 9747 AG Groningen, The Netherlands. E-mail: p.rudolf@rug.nl*
[b] *Department of Materials Science & Engineering, University of Ioannina, 45110 Ioannina, Greece*
[c] *Laboratory of Industrial Chemistry, Department of Chemistry, University of Ioannina, 45110 Ioannina, Greece. E-mail: terzoi@uoi.gr*
[d] *Digital Manufacturing and Materials Characterization Laboratory, School of Science and Technology, International Hellenic University, 14 km Thessaloniki, 57001 N. Moudania, Greece*
[e] *Biotechnology Laboratory, Department of Biological Applications and Technologies, University of Ioannina, 45110 Ioannina, Greece*
[f] *School of Chemical and Environmental Engineering, Technical University of Crete, 73100 Chania, Crete, Greece*
[g] *Laboratory of Polymers and Colours Chemistry and Technology, Department of Chemistry, Aristotle University of Thessaloniki, GR-54124 Thessaloniki, Greece*
† Present address: Department of Chemistry, University of Ioannina, GR 45110, Ioannina, Greece.
‡ Present address: Department of Chemistry, University of Crete, GR-70013, Heraklion, Crete, Greece.

Germanane has been reported to possess significant antibacterial activity against both Gram-negative and Gram-positive bacterial strains.[18] Despite the intrinsic mechanical deficiencies of PLA, its potential in food packaging applications increases significantly when stabilized or enriched with antioxidants.[19–21] Other polymer-based nanocomposites have been reported as efficient carriers for antioxidants[22,23] or for skin and bone tissue engineering.[24,25] Among these properties, antimicrobial activity is particularly important for biomedical applications. To date, antimicrobial polymeric nanocomposites reinforced with graphene derivatives[26] or copper[27] have been reported; however, studies on polymer-based nanocomposites incorporating functionalized germanene remain scarce. Feng *et al.*[28] prepared hydrogel-based nanocomposites with drug-loaded PEGylated Ge nanosheets for cancer treatment, demonstrating efficient postoperative wound coating and excellent theranostic properties.

PLA/GeH nanocomposites are thus promising for applications requiring combined mechanical reinforcement and bioactivity, such as bioactive packaging and biomedical devices. This study addresses this knowledge gap by evaluating the structural, thermal, crystallization, mechanical, and bioactive properties of PLA/GeH nanocomposites. To explore GeH as a nanofiller for PLA, nanocomposites with different GeH content (0.5, 1.0, 2.0, 3.0, and 5.0 wt%) were prepared by solution casting. The nanocomposites are hereafter referred to as PLA/GeH 0.5, PLA/GeH 1.0, PLA/GeH 2.0, PLA/GeH 3.0, and PLA/GeH 5.0. The effects of the GeH nanosheets on the physicochemical, mechanical, and crystallization properties of PLA were investigated using Fourier transform infrared (FTIR) spectroscopy, X-ray diffraction (XRD), thermogravimetric analysis (TGA), differential scanning calorimetry (DSC), energy-dispersive X-Ray spectroscopy (EDS), and nanoindentation. Transmission electron microscopy (TEM) and scanning electron microscopy (SEM) were employed to examine the morphology and structure of the nanocomposites. Finally, the biological properties of the prepared nanocomposites were evaluated, including their antioxidant activity *via* ABTS and DPPH radical scavenging assays and their antimicrobial activity against *Escherichia coli* (BL21(DE3)) and *Corynebacterium glutamicum* (ATCC 21253).

2. Experimental section

2.1. Materials and reagents

Calcium (granular Ca with 99% purity), germanium (Ge powder with 99.999% purity), ethylenediaminetetraacetic acid disodium salt dihydrate (EDTA Na_2, ACS reagent 99.0–101.0%), potassium persulfate, 2,2-azino-bis(3-ethylbenzthiazoline-6-sulfonic acid) (ABTS) and 2,2-diphenyl-1-picrylhydrazyl (DPPH) were purchased from Sigma-Aldrich; ethanol (EtOH, analysis grade), tetrahydrofuran (THF, reagent grade), and hydrofluoric acid (HF, 38–40% w/w solution) were acquired from Merck. Milli-Q water with a resistivity of 18.2 MΩ cm was used in this work. Poly(lactic acid) (PLA) Ingeo™ Biopolymer 2003D (D-isomer 4%, M_n = 106 700 g mol^{-1} and M_w = 180 300 g mol^{-1} (SEC), specific gravity 1.24 g per cc, melt flow rate (MFR) 6 g/10 min at 210 °C) from Natureworks was kindly donated by Plastika Kritis S.A. LB Broth Lennox was purchased from NEOGEN and sodium chloride from Riedel de Haen. All other chemicals were of reagent grade and purchased from Sigma-Aldrich.

2.2. Synthesis and characterization of GeH

Germanane was synthesized based on our previously published protocol, where β-$CaGe_2$ was topotatically deintercalated in an aqueous HF solution (Merck, 38–40% w/w) at room temperature for a few minutes.[18] The synthesized product was characterized with a series of techniques such as X-ray diffraction (XRD), Fourier transform infrared (FTIR) and Raman spectroscopy, atomic force (AFM) and scanning electron (SEM) microscopy in order to verify that the obtained material had the desired structure and chemical composition.

2.3. Preparation of nanocomposites

Germanane was thermally treated at 200 °C under N_2 atmosphere for 1 h prior to its use for the preparation of the PLA nanocomposites in order to remove any residual physisorbed water and other organic contaminants. The PLA/GeH nanocomposites were prepared by solution casting; first, a predetermined mass of GeH nanosheets was dispersed in tetrahydrofuran in a concentration of 2 mg mL^{-1} by stirring for 30 min, followed by sonication for 30 min with a Hielscher UP100H ultrasonic processor (100 W, 30 kHz) set at 80% intensity. The mass of GeH nanosheets corresponded to 0.5, 1.0, 2.0, 3.0 and 5.0 wt% GeH content. Each GeH dispersion was mixed with a 3.0% w/v solution of PLA in dichloromethane. After stirring for 1 h, the mixtures were poured into crystallizing dishes. The solvents were left to evaporate for 24 h at room temperature, followed by 24 h of drying under vacuum at 50 °C (Scheme 1). Neat PLA was also solvent cast. The final

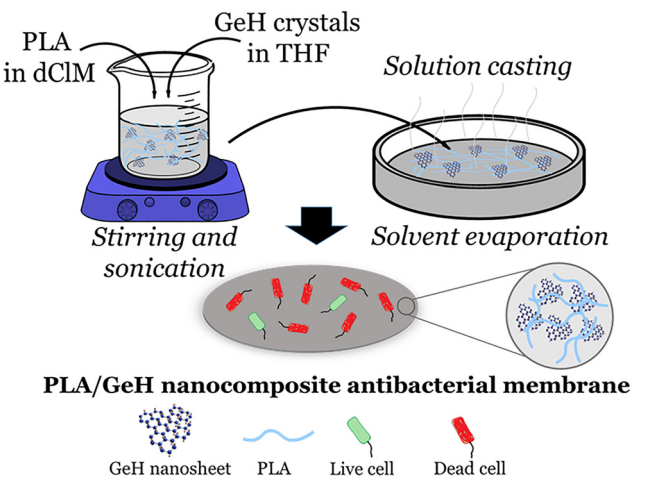

Scheme 1 Schematic representation of the experimental procedures followed for the fabrication of the PLA/GeH nanocomposites and the evaluation of the bactericidal properties.

concentration of GeH in the nanocomposites was quantified by thermogravimetric analysis, as described in 2.4.

2.4. Characterization of GeH and PLA/GeH nanocomposites

Scanning electron microscopy images of GeH were obtained using a JEOL JSM-6510 LV SEM Microscope (JEOL Ltd, Tokyo, Japan) equipped with an X-Act EDS detector by Oxford Instruments (acceleration voltage 20 kV) for elemental analysis and mapping. The specimens were covered with a thin (4–8 nm) Au–Pd film using a mini sputter coater SC7620 from Quorum Technologies LTD (Kent, UK).

Atomic force microscopy images of GeH were obtained in AC mode using an Asylum Cypher-S instrument, Asylum Research, with HQ-300 Au-coated cantilevers with a tip radius of 10 nm, spring constant of 40 N m^{-1} and operating frequency of 300 kHz. Exfoliated GeH nanosheets were drop casted onto silicon wafers (P/Bor, single side polished, purchased from Si-Mat) from ethanol dispersions.

The FTIR spectrum of GeH was acquired with a Shimadzu FTIR 8400 spectrometer equipped with a deuterated triglycine sulfate (DTGS) detector in the range of 400–4000 cm^{-1}, averaging 32 scans collected with 2 cm^{-1} resolution. The sample was in the form of a KBr pellet containing *ca.* 2 wt% of GeH. FTIR spectra of PLA/GeH thin films, prepared by spin-coating onto SiO_2 substrates, were collected using a PerkinElmer SPECTRUM 1000 FTIR spectrometer. The resolution was 2 cm^{-1}, and the number of co-added scans in each spectrum was 16; the spectra presented were baseline-corrected and converted to absorbance mode. Raman spectra of GeH were obtained using a Labram Horiba HR spectrometer with a laser excitation wavelength of 514 nm; the laser power of 1.5 mW was focused onto a 2 μm spot.

The XRD pattern of GeH was collected on a D8 Advance Bruker diffractometer with Cu Kα radiation (40 kV, 40 mA) and a secondary-beam graphite monochromator. The pattern was recorded in the 2θ range of 10–65°, in steps of 0.02°, and a counting time of 2 s per step. XRD measurements of the nanocomposites were performed over the 2θ range of 5 to 60°, in steps of 0.05°, scanning speed 1° min^{-1}, using a MiniFlex II XRD system from Rigaku Co. with Cu Kα radiation (λ = 0.154 nm). Transmission electron microscopy (TEM) was performed using a JEOL JEM HR-2100 instrument, operated at 120 keV. The drop-casted PLA-GeH5.0 film was cryo-ultramicrotomed using a a Leica EM UC7, producing (~40 nm thin sections) that were picked up on 600-mesh copper TEM grids for immediate observation.

Themogravimetric analysis (TGA) was carried out with a Setaram Setsys TG-DTA 16/18 instrument. Samples (8 ± 0.2 mg) were placed in alumina crucibles; a blank measurement was performed and subsequently subtracted from the experimental curves of GeH and of the PLA/GeH nanocomposites to correct for buoyancy effect. The nanocomposite samples were heated from ambient temperature up to 600 °C with a heating rate of 20 °C min^{-1}, while GeH samples were heated up to 1000 °C, under a 50 mL min^{-1} N_2 flow. Both sample temperature and sample weight were continuously recorded.

Differential scanning calorimetry (DSC) studies were performed using a PerkinElmer (Shelton, Connecticut, USA) Pyris Diamond DSC calorimeter under a nitrogen gas flow of 50 mL min^{-1}. The instrument was calibrated with indium for the accurate determination of heat flow and temperature. A sample mass of 5.00 mg was used for all tests; the sample and reference pans were of identical mass within ±0.01 mg. The degree of crystallinity (X_c) was calculated with eqn (1):

$$X_c\ (\%) = \left(\frac{\Delta H_m}{\Delta H_f^0 \times \left(1 - \frac{\text{additive wt\%}}{100}\right)} \right) \times 100 \qquad (1)$$

where ΔH_m is the experimental melting enthalpy and ΔH_f^0 the theoretical heat of fusion of 100% crystalline PLA (ΔH_f^0 = 93 J g^{-1}).

Isothermal crystallization from the melt experiments were performed at temperatures from 97.5 to 107.5 °C. PLA was first melted at $T = T_m + 40$ °C for 5 min to erase all thermal history and then cooled at a rate of 200 °C min^{-1} to the desired crystallization temperature. After holding isothermally until crystallization was complete, a heating step with a rate of 20 °C min^{-1} to $T = T_m + 40$ °C followed.

The mechanical performance of the PLA/GeH nanocomposites was investigated *via* nanoindentation testing. The samples were indented with a 100 nm radius triangular pyramidal tip (Berkovich – type indenter) mounted on a dynamic ultra-microhardness tester (DUH-211; Shimadzu Co., Kyoto, Japan). These tests precisely measure local variations of elastic modulus and hardness;[29–31] the load of the indenter was recorded as a function of the indentation depth. The measurements were carried out in five different points on the surface of each film, with a holding time of 3.0 s at both load and unload. Nanoindentation tests were performed in the load-control mode at a peak load of 50 mN. During the creep time the maximum indentation load was applied to the indenter; the change in indentation depth (displacement) was monitored as a function of time and subsequently the indenter was unloaded until zero load.

The antioxidant activity of the PLA surfaces was evaluated based on the DPPH and ABTS radical scavenging assays,[32–34] PLA and PLA/GeH nanocomposite films of approximately 0.25 cm^2 were immersed in ethanolic $DPPH^•$ solution (0.03 mM) and left at RT. Measurements were conducted using spectrophotometry at 517 nm, with ethanol as the blank. For the ABTS assay, PLA and PLA/GeH nanocomposite films (0.25 cm^2) were immersed in aqueous $ABTS^{•+}$ solution adjusted to a final absorbance of 0.7 ± 0.05, and incubated at room temperature for different time intervals (30, 60, 120, 240 min). The decrease in absorbance of the $ABTS^{•+}$ solution was measured at 734 nm using a UV/vis microplate reader (Multiskan SkyHigh, Thermo Fisher Scientific, Cleveland, OH, USA). All experiments were conducted in triplicate and results are expressed as mean ± standard deviation. The radical scavenging activity (RSA) was calculated according to the following

equation (eqn (2)):

$$\text{RSA}\ (\%) = \frac{A_{\text{control}} - A_{\text{sample}}}{A_{\text{control}}} \times 100 \qquad (2)$$

where A_{control} is the absorbance of the control, and A_{sample} is the absorbance of each PLA surfaces.

Statistical analysis was performed by analysis of variance (ANOVA). Multiple comparisons of means (Dunnett's and Tukey's tests) were conducted to identify significant differences, which were considered at $p < 0.05$, using IBM SPSS Statistics version 21 (SPSS Inc., Chicago, IL, USA).

The antibacterial activity of the PLA/GeH nanocomposite films was tested against a Gram-negative strain (*Escherichia coli-E. coli*) and a Gram-positive one (*Corynebacterium glutamicum-C. glutamicum*), as previously reported.[33] In brief, a fresh bacterial inoculum was prepared by incubating bacterial cells overnight in sterile Lysogeny Broth (LB) at 37 °C with shaking. An exponential-phase bacterial population corresponding to $\approx 10^7$ CFU mL^{-1} was then prepared in 0.9% NaCl solution (w/v), and 100 μL was added to Eppendorf tubes containg 0.25 cm^2 of each film, followed by incubation for 18 h in a cold chamber. Control samples consisted of 100 μL of bacteria incubated without a nanocomposite film. After 18 h, 25 μL from each sample were transferred to a 96-well Elisa microplate containing 225 μL of LB medium. The microplate was incubated at 37 °C for 8 h with continuous stirring, and bacterial growth was determined by measuring the Optical Density (O.D.) at 600 nm at 1 h intervals. The % lethal effect of each sample was calculated according to the following equation (eqn (3)):

$$\text{Lethal effect}\ (\%) = \frac{\text{O.D.}_{\text{control}} - \text{O.D.}_{\text{sample}}}{\text{O.D.}_{\text{control}}} \times 100 \qquad (3)$$

where O.D.$_{\text{control}}$ is the optical density of the control at 600 nm, and O.D.$_{\text{sample}}$ the optical density of each sample at 600 nm in the exponential growth phase. All measurements were performed at least in duplicate.

3. Results and discussion

3.1 Characterization of GeH

Powder XRD measurements were performed to determine the crystal structure of the pristine germanane. The characteristic diffraction peaks in the pattern (see Fig. 1(a)) at 2θ = 17, 27 and 45° originate respectively from the (002), (100), and (110) crystallographic planes and are in agreement with our previous study.[17]

To further elucidate the structure and the chemical composition of the pristine GeH, Raman and FTIR spectra were recorded. Raman spectrum of GeH (Fig. 1(b)) is dominated by an intense peak at 287 cm^{-1}, which corresponds to the E_{2g} in-plane vibration mode of the Ge atoms in the honeycomb lattice of GeH.[16,17] In the FTIR spectrum of germanane (Fig. 1(c)) the

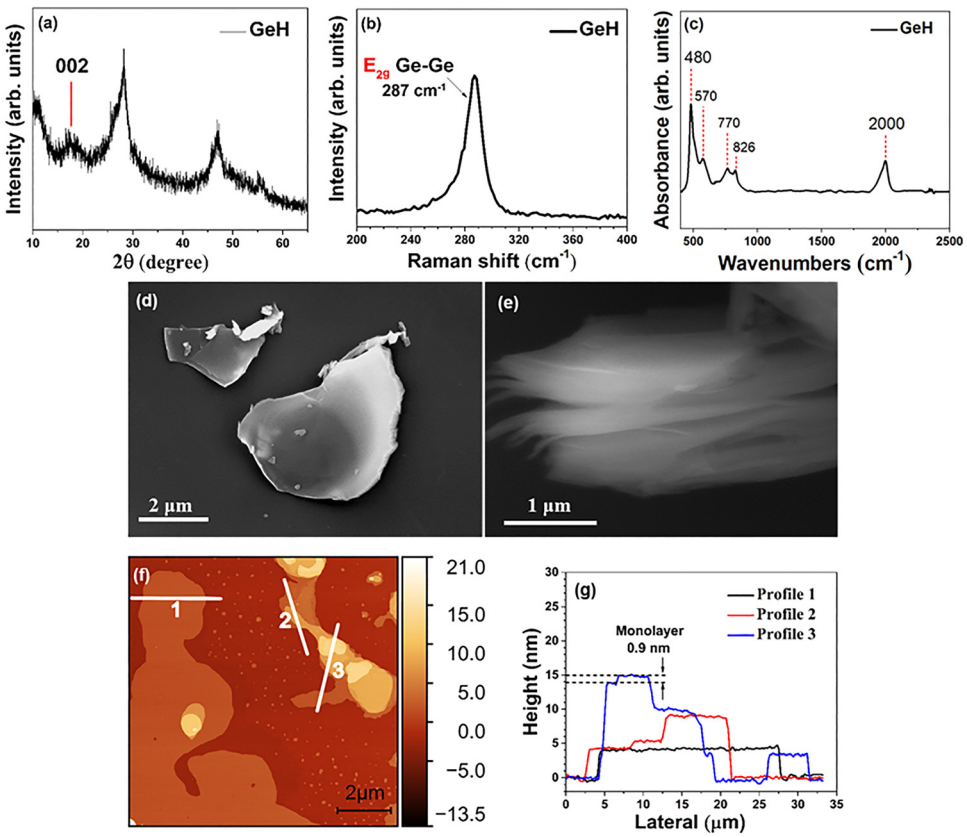

Fig. 1 Characterization of the synthesized germanane – (a) XRD pattern; (b) Raman and (c) FTIR spectra; (d) and (e) SEM and (f) AFM images along with (g) height profiles of the individual exfoliated nanoflakes drop casted from ethanol dispersions onto SiO_2 substrates.

strong peak at 2000 cm^{-1} that derives from the Ge–H stretching vibration, as well as the signature of the Ge–H wagging modes at 480 and 584 cm^{-1} confirm that the germanium atoms are hydrogenated.[16,17] In addition, the weak peaks at 770 and 830 cm^{-1} stem from H–Ge–H bending modes of neighboring H-terminated germanium atoms at the edges of the crystalline layers and/or next to Ge vacancies in the germanane lattice.[16,17] Scanning electron and atomic force microscopy images revealed the layered structure of the GeH crystallites. Both panels, (d and e) in Fig. 1 present the SEM observations of different GeH flakes. Fig. 1(d) shows two distinctive GeH crystallites (top view), while Fig. 1(e) shows the side view of another GeH crystal, highlighting the layered nature and the accordion-like structure of the sample. Fig. 1(f) present the AFM image of different exfoliated individual GeH nanosheets and their height profile analysis is presented in Fig. 1(g). The thickness of a single layer germanane was found to be 0.9 nm ± 0.1 nm, in agreement with previous studies.[17]

3.2 Characterization of PLA/GeH nanocomposites

3.2.1. Dispersion and structural characterization. The surface and the cross section of the as-prepared bulk nanocomposites PLA/GeH were examined with SEM, and representative images of neat PLA, PLA/GeH 0.5, PLA/GeH 2.0, and PLA/GeH 5.0 nanocomposite bulk samples as obtained after crystallization are presented in Fig. 2. The micrographs clearly show that the GeH nanosheets affect the final morphology of the nanocomposite. Neat PLA (Fig. 2(a) and (a_i)) exhibits a homogeneous surface and its cross section a non-ordered holey structure. When GeH is incorporated at low concentration (0.5 wt%) (Fig. 2(b) and (b_i)), spherulitic structures emerge on the surface and the cross section of the composite film displays a denser and more compact morphology due to solvent-induced crystallization. This trend persists for higher amounts of GeH as seen in Fig. 2(c) and (c_i) for PLA/GeH 2.0, and Fig. 2(d) and (d_i) for PLAGeH 5.0, where similarly to PLA/GeH 0.5 different spherulites are apparent on the surface and the cross section always presents a significantly denser and more compact structure than pure PLA. The denser morphology (higher nucleation density) observed for PLA/GeH 2.0 likely resulted from solvent-induced crystallization during sample preparation, where the evaporation rate was uncontrolled and likely varied between samples. These findings testify to the role of the nanofiller (GeH) as nucleation site for PLA crystallization. Since GeH has a layered structure and can be exfoliated in few-layered flakes or even single layers,[17,18] it provides more active sites, which will act as nucleation centers during the crystallization process of the PLA/GeH composite.

For the cross section of the PLA/GeH 5.0 nanocomposite, shown in Fig. 3(a), energy-dispersive X-ray spectroscopy (EDS) data were acquired, and are presented in Fig. 3(b). The elemental mapping shown in Fig. 3(a_i)–(a_{iv}) indicates that the Ge signal clearly overlaps everywhere with the carbon and oxygen signals coming from $(C_3H_4O_2)_n$. This observation confirms both the successful incorporation of GeH and the uniform distribution of the nanofiller in the PLA matrix. In the EDS elemental

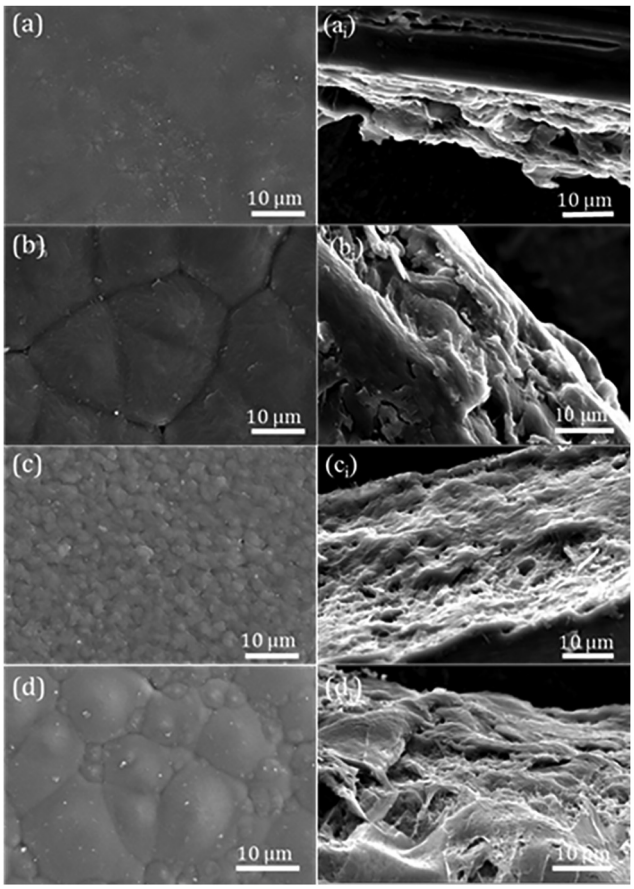

Fig. 2 SEM images of the surface (left) and the cross section (right) of bulk samples of (a) and (a_i) neat PLA; (b) and (b_i) PLA/GeH0.5; (c) and (c_i) PLA/GeH2.0 and (d) and (d_i) PLA/GeH5.0.

mapping of Ge (Fig. 3(a_{iii})) one also notices a few high intensity spots, which point to the presence of not perfectly exfoliated flakes of GeH. Fig. 3(c) and (d) present the TEM images of the nanocomposite PLA/GeH 5.0. The images show homogeneously dispersed, exfoliated GeH incorporated in the PLA polymer matrix (parts identified with white ovals in Fig. 3(d)). However, careful observation of the microtomed sections in TEM revealed again not completely exfoliated GeH flakes as identified in Fig. 3(d) with a red oval.

To determine whether any specific bonds are formed between PLA and the GeH nanosheets in the composite, FTIR spectra were recorded (Fig. S1(a)). The main bands in the spectrum of PLA are observed at 3507 cm^{-1} (O–H stretching), 2995 cm^{-1} (–CH_3 asymmetric stretching), 2945 cm^{-1} (–CH symmetric stretching), 1757 cm^{-1} (C═O stretching), 1453 cm^{-1} (–CH_3 bending), 1382 cm^{-1} (–CH_3 scissor mode), 1184 cm^{-1} (C–O stretching), and 1090 cm^{-1} (C–CH_3 stretching).[35] The positions of the FTIR bands remain unchanged after the incorporation of GeH, indicating that no new bonds were formed between the polymer and the nanofiller.

The X-Ray diffraction patterns of bulk films of both PLA and its nanocomposites, shown in Fig. S1(b), reveal an amorphous

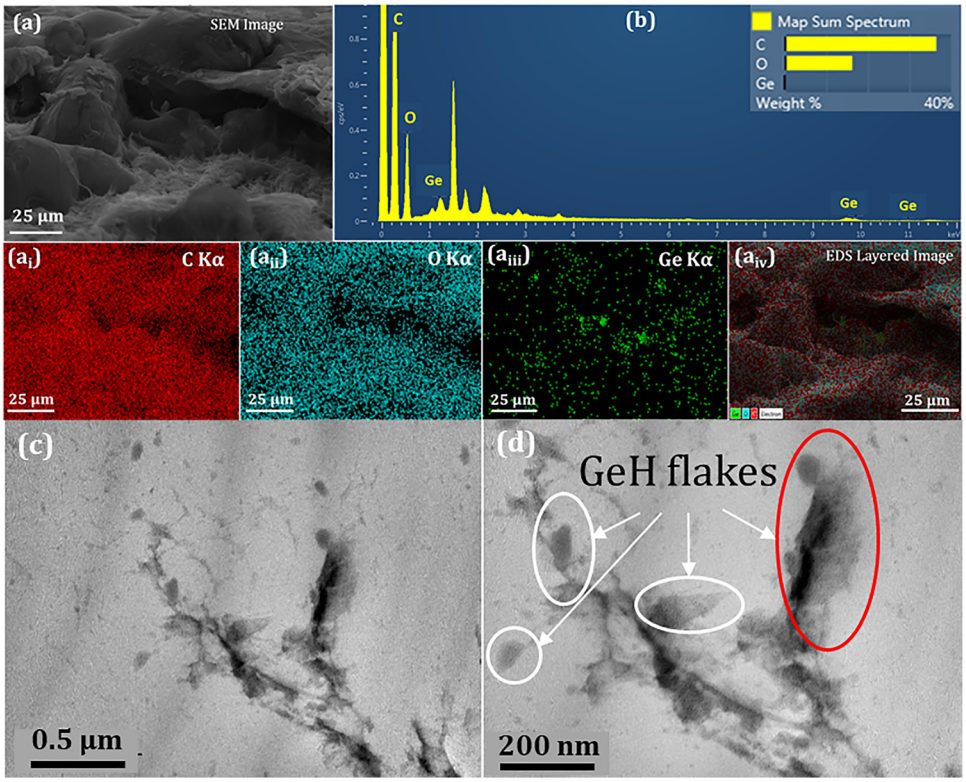

Fig. 3 SEM, EDS mapping and TEM images of the PLA/GeH 5.0 bulk: (a) SEM image obtained in the cross section of the film; (b) EDS spectra and elemental mapping (a_i)–(a_{iii}) along with the combined EDS layered image (a_{iv}); (c) and (d) TEM images of the PLA/GeH 5.0.

structure in all cases, with the typical broad halo at 15–20°. This result is expected given the high molecular weight of the PLA used and its very slow crystallization rate. Notably, a small peak appears at 27.7° upon addition of GeH nanosheets, and its intensity increases with higher GeH content. Since GeH nanosheets are highly crystalline, the reflections at ~17° and 27.7° correspond to the (002) and (001) crystallographic planes, respectively.[16,17] The (002) peak is barely visible in the nanocomposites with low nanofiller content, likely because too few non-exfoliated GeH flakes were present to give rise to a measurable signal, but it is clearly seen in the sample with 5 wt% nanofiller. This suggests that the degree of exfoliation of the nanofiller seems is influenced by its concentration in the nanocomposite. The presence of non-exfoliated GeH flakes in the PLA matrix agrees with the TEM and the SEM findings presented in Fig. 3.

3.2.2. Thermal properties and crystallization. Differential scanning calorimetry studies were performed for the determination of the characteristic thermal transitions of the as-prepared bulk samples. The curves from the first and second heating after quenching are shown in Fig. S2. No crystallization peak was detected during cooling from the melt at 10 °C min^{-1}, due to the high molecular weight of PLA. The effects of GeH nanosheets on the melting point (T_m), glass transition temperature (T_g), and crystallinity (X_c) are presented in Fig. 4. During the first heating, T_m varied with GeH content, but after erasing the thermal history (second heating), it was ~149 °C regardless of filler content. Similarly, T_g was ~61 °C during the second heating, independent of GeH content. The degree of crystallinity of the as-prepared samples (data from 1st heating scan, Fig. S2(a)) increased from 22% in neat PLA to a maximum

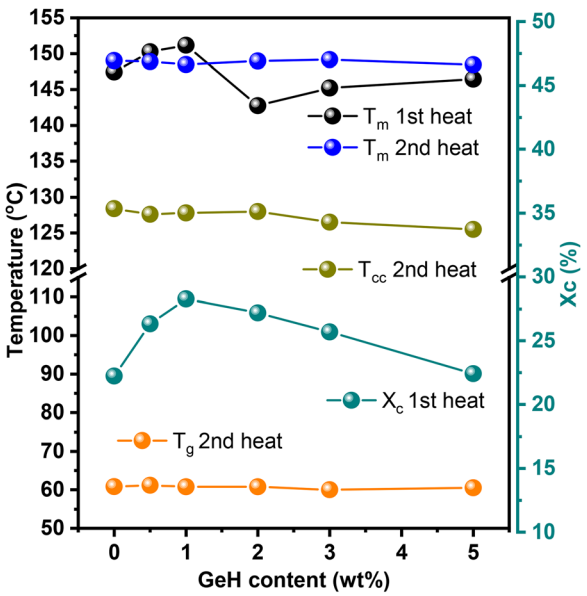

Fig. 4 Effect of GeH content on the melting point, T_m, the glass transition temperature, T_g, and the crystallinity X_c of PLA.

of 28% in PLA/GeH 1.0, suggesting that GeH nanosheets act as heterogeneous nucleation agents, in agreement with the increased nucleation density observed by SEM. Cold crystallization during the 2nd heating scan of Fig. S2(c) is almost undetectable in neat PLA but becomes more pronounced in the nanocomposites. The weak peaks indicative of cold crystallization (Fig. S2(c)) gradually shift to slightly lower temperatures, and their area significantly increases along with the consequent melting of the formed crystals, likely due to the nucleating effect of GeH nanosheets.[36]

The resulting mass (%)–temperature curves and differential thermogravimetric analysis (DTG) graphs from TGA are depicted in Fig. S3. The characteristic peak temperature of the DTG curve, where decomposition occurs at the fastest rate (T_p), together with the percentage of char residue, are presented in Table 1. A first mass loss of 2–5%, depending on GeH content, is barely perceptible in neat PLA but clearly visible in the nanocomposites, occurring at $T_p \approx 150$ °C. This loss corresponds to the release of residual solvent from solution casting. The main degradation of PLA takes place in a single step between 350 and 400 °C. The nanocomposites follow a similar trend but with a slightly reduced T_p. This small decrease in thermal stability may result from the lack of strong interactions between the PLA matrix and GeH nanosheets.[37,38] The solid residue increases with higher GeH content, as expected due to the inorganic nature of the latter.

The crystallinity of the polymer in the nanocomposite not only affects the optical properties but also directly influences the processing when manufacturing different items such as films and bottles. Crystallization of PLA is essential before drying the pellets to avoid clumping, or after molding into components to enhance mechanical performance. Increasing the crystallinity not only improves barrier properties but also stabilizes the shape of PLA-based items.[39] PLA of medium to high molecular weight crystallizes very slowly;[39–43] according to the manufacturer, the optimum conditions for the crystallization of PLA 2003D, used in this study, are 88–99 °C for 10–20 min. Nanoparticles are known for their ability to accelerate polymer crystallization by acting as heterogeneous nucleation agents, thereby increasing the nucleation density of PLA.[40,44–47]

The isothermal melt crystallization kinetics of the PLA nanocomposites were studied at crystallization temperatures between 97.5 and 107.5 °C. The resulting differential scanning calorimetry curves recorded during the isothermal step and subsequent melting are presented in Fig. S4 and S5, respectively. The evolution of the relative crystallinity, $X_{(t)}$, of neat PLA and its composites as a function of time at different crystallization temperatures is displayed in Fig. S6. Fig. 5(a), presents the inverse of the crystallization half time, $t_{1/2}$, defined as the time required for a sample to reach 50% of its total crystallinity, while Fig. 5(b) shows the final X_c for neat PLA and the nanocomposites. The $t_{1/2}$ of PLA ranged from 26 to 34 min (Table S1), in good agreement with previously reported values for PLA with the same D-isomer content and similar molecular weight.[43,48] The spherulite growth rate of PLA is known to reach a minimum when the molecular weight is $\geq 100\,000$ g mol^{-1} because of restricted chain mobility.[40] For neat PLA, both the time to peak and $t_{1/2}$ increased slightly with temperature, although the effect was not significantly. By contrast, the nanocomposites especially those containing 0.5–3.0 wt%-consistently exhibited lower $t_{1/2}$ values across the temperature range. Adding 0.5, 1.0 and 3.0 wt% GeH reduced the $t_{1/2}$ of PLA by about 5 min in the temperature range 97.5–102.5 °C, probably because the GeH nanosheets act as nucleation agent. Conversely, $t_{1/2}$ was not greatly affected after the incorporation of 5.0 wt% GeH, likely due to the presence of aggregates. Consequently, the nanocomposites with GeH content between 0.5 and 3.0 wt% showed an increased X_c by approximately 2–4% after melt crystallization in the 97.5–102.5 °C range (Fig. 5(b)), whereas the effect was less pronounced at higher temperatures. The decrease of crystallinity in the presence of 5.0 wt% GeH can be a consequence of confinement, supported by X_c dropping to ~21–23%.[49] This trend suggests that at higher filler loadings, the GeH flakes may hinder chain mobility and hinder crystalline growth.

The isothermal crystallization kinetics were analyzed with the Avrami method (detailed in the SI). The effect of the melt crystallization temperature and of the presence of the fillers on the Avrami exponent n and the growth function k is shown in (Fig. 5(c) and (d)). Herein, the Avrami exponent n ranged between 1.90 and 2.35 (Fig. 5(c)) and slightly increased with crystallization temperature. The presence of 0.5–3.0 wt% GeH generally led to higher n values, implying a shift toward more complex (likely 3D) crystal growth with simultaneous heterogeneous nucleation.[43] For PLA/GeH 5.0, a lower n value was observed, consistent with the longer $t_{1/2}$ times and lower crystallinity. This suggests that high filler loadings might hinder crystallization due to confinement and reduced chain mobility.[49–57]

The crystallization rate constant k (Fig. 5(c)) also increased with the addition of 0.5–3.0 wt% GeH, indicating faster crystallization, again confirming the role of GeH as a nucleation agent.[45,58–61] Both k and the inverse $t_{1/2}$ (Fig. 5(a) and (c)) followed a similar trend, generally decreasing at higher temperature. The highest crystallization rate was observed at 100 °C in the PLA/GeH 3.0 wt% sample. The layered structure of GeH provides a high specific surface area that facilitates heterogeneous nucleation by offering planar surfaces on which PLA chains can adsorb, align and crystallize. This geometry-driven nucleation is more effective than simply serving as a physical barrier, as it promotes oriented crystal growth and accelerates

Table 1 Thermal degradation characteristics of PLA and its nanocomposites with GeH

Sample	T_p (°C)	Residue at 600 °C (wt%)
PLA	387.6	0.88
PLA/GeH 0.5	383.1	1.06
PLA/GeH 1.0	375.2	1.56
PLA/GeH 2.0	380.8	1.80
PLA/GeH 3.0	371.7	2.55
PLA/GeH 5.0	375.6	3.75

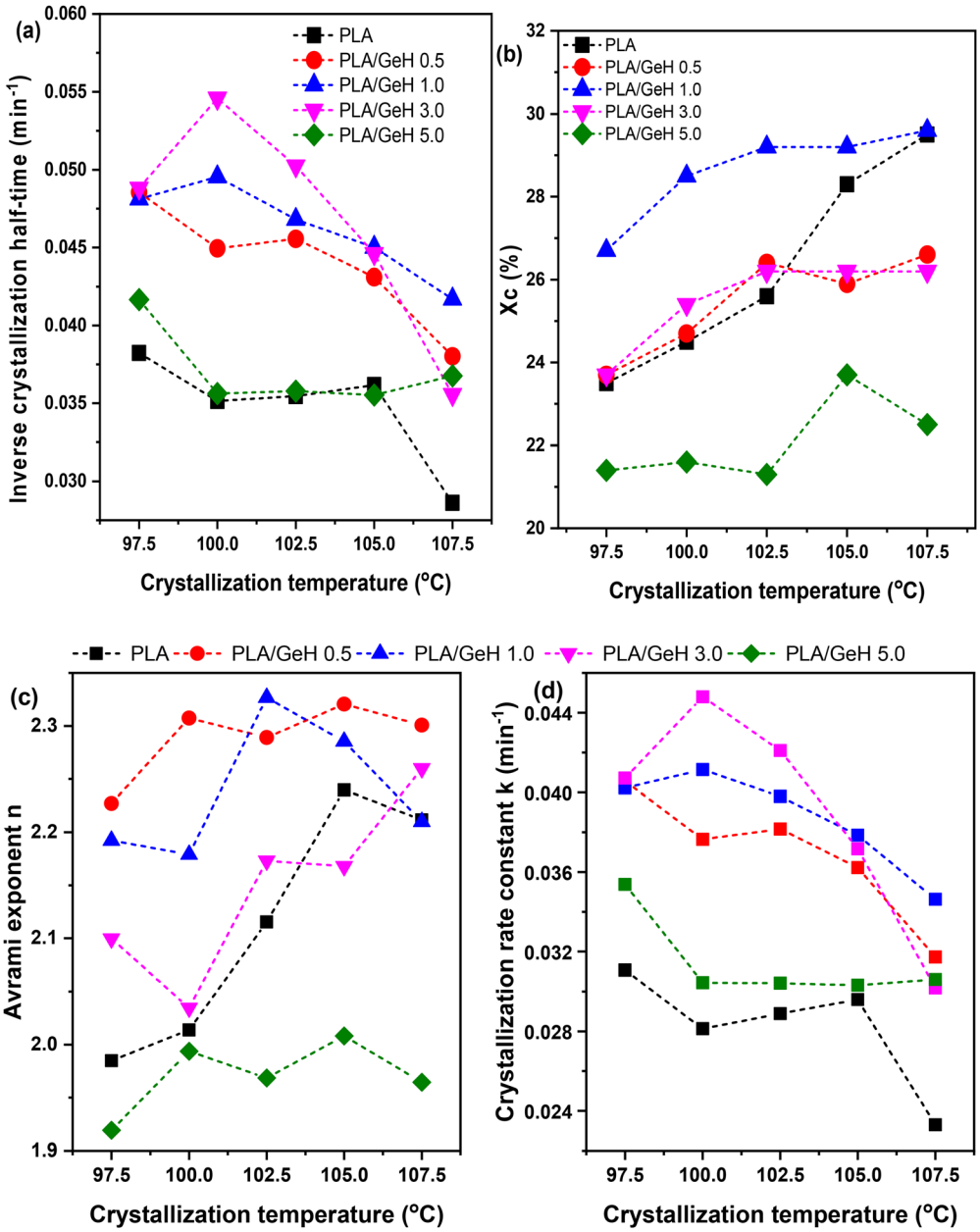

Fig. 5 Effect of GeH nanosheet content and crystallization temperature on the (a) inverse crystallization half-time $t_{1/2}$, (b) percentage of crystallinity X_c of PLA during isothermal melt crystallization, (c) Avrami exponent, n, and (d) the crystallization rate constant, k, of PLA; the behavior of neat PLA is plotted in each case for comparison. The lines are to guide the eye.

spherulite formation without significantly affecting T_g or T_m. At higher loadings ($\geq$5 wt%), aggregation reduces the effective surface area, diminishing nucleation efficiency and slightly limiting the crystallinity enhancement.

Although no clear evidence of hydrogen bonding between PLA ester –C═O groups and GeH nanoadditives was observed in the FTIR spectra, the thermal analyses suggest that weak noncovalent interactions occur. These interactions appear sufficient to promote nucleation, leading to faster crystallization and slightly higher crystallinity at low GeH loadings (0.5–3 wt%), while having minimal impact on T_g, T_m, and overall thermal stability. Despite their low strength, these interactions help maintain the stability of the composites and prevent significant migration of the nanosheets under normal conditions. Consequently, PLA/GeH nanocomposites could prove suitable for applications requiring moderate thermal and mechanical performance, such as bioactive packaging and biomedical devices.

3.2.3. Mechanical properties. The mechanical behavior of the neat PLA and the PLA/GeH nanocomposites was determined using nanoindentation. These tests were performed following ISO 14577 standards. (Note: due to its low melt flow rate (MFR = 6 g/10 min at 210 °C) and resulting high viscosity, the PLA used could not form uniform compression-molded

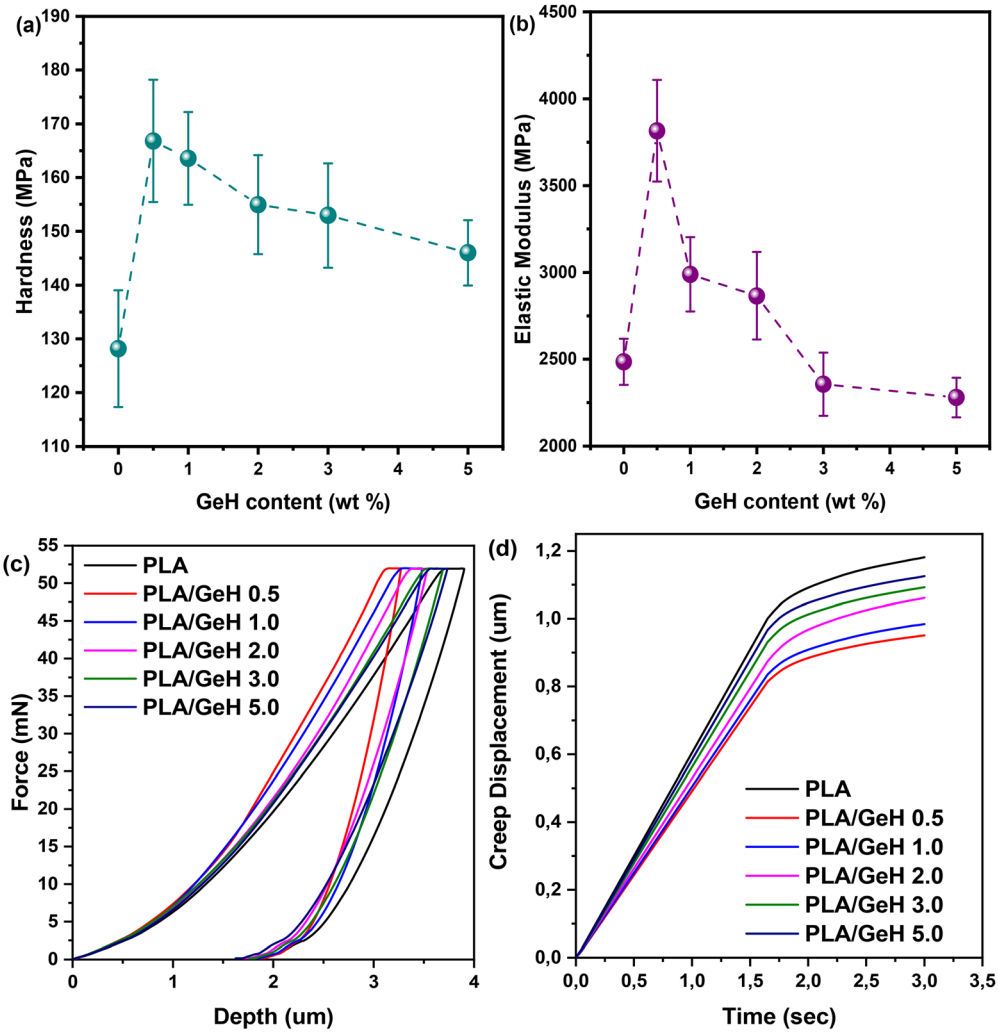

Fig. 6 Comparison of the (a) hardness; (b) elastic moduli; (c) typical load-depth nanoindentation curves and (d) representative creep displacement–time curves for neat PLA and PLA/GeH with various concentrations of the nanofiller.

films suitable for standard tensile testing; therefore, tensile strength measurements were not performed.) Fig. 6 summarizes the average values of hardness and elastic modulus as a function of GeH concentration as derived from these tests, the comparison of the load – depth curve of neat PLA with those of the PLA/GeH composites, and the creep displacement at the peak force of 50 mN as a function of time. The hardness of PLA/GeH samples (Fig. 6(a)) improved with increasing GeH content compared to neat PLA. The highest value, 166.2 MPa, was achieved with the addition of 0.5 wt% GeH, representing an ~30% increase compared to neat PLA (128.2 MPa). Higher GeH contents also increased the hardness but to a lesser extent: by around 28% for 1.0 wt%, 21% for 2.0 wt%, 19% for 3.0 wt% and 14% for 5.0 wt% GeH. The lower hardness values for 1.0–5.0 wt% GeH could be related to nanoplatelet aggregation.

The elastic modulus (Fig. 6(b)) for neat PLA was 2484.8 MPa. The addition of 0.5 wt% GeH increased the modulus to 3815.3 MPa, which corresponds to 53% enhancement compared to neat PLA. Adding 1.0 and 2.0 wt% GeH to PLA also increased the elastic modulus by 20% and 15%, respectively. In contrast, PLA with 3.0 wt% and 5.0 wt% GeH exhibited elastic moduli that were 5% and 8% lower than that of neat PLA. This decrease can be attributed to agglomeration of the nanofiller within the PLA matrix.

Fig. 6(c) compares the load-depth curves of neat PLA and PLA/GeH nanocomposites as obtained from the nanoindentation tests. As expected from the hardness results, the indentation depths were highest for neat PLA (3.53 to 3.90 μm) and lowestfor PLA/GeH 0.5 (3.12 to 3.28 μm), while the other PLA/GeH samples showed intermediate values. Fig. 6(d) illustrates the creep displacement at the peak force of 50 mN as a function of time. The creep displacement is the difference between the indentation depth at the moment when the peak load of 50 mN is reached and the indentation depth at the end of holding time under constant load. The variation of the creep displacement with holding time confirms that the addition of GeH has a positive impact on the hardness since the creep displacement was significantly reduced compared to neat PLA. It seems that

the GeH nanosheets act as blocking sites, hindering the movement of polymer chains subjected to the deformation field. This effect becomes particularly evident at higher GeH concentrations, where the nanoplatelets restrict the viscous flow of PLA. Moreover, the significant reduction in creep displacement even at the highiest GeH concentration demonstrates efficient load transfer between the PLA matrix and the nanomaterial, which is at the origin of the good creep resistance of the nanocomposites. While the solvent-induced dense spherulites observed by SEM may contribute to mechanical behavior, the systematic trends in hardness, elastic modulus, and creep resistance showed correlation with GeH content and dispersion.

3.3. Biological activity of PLA/GeH nanocomposites

The antioxidant activity of PLA/GeH nanocomposites was determined by monitoring the color quenching of the synthetic radicals DPPH and ABTS. As expected, neat PLA films exhibited minimal radical-scavenging capacity (Fig. 7(a) and (b)); however, incorporation of GeH significantly enhanced the antioxidant activity of the nanocomposites, with the effect being both dose- and time-dependent. At the highest GeH loading (5 wt%), the DPPH$^{\bullet}$ and ABTS$^{\bullet+}$ scavenging activities reached 57.3 and 93.5% after 240 min, respectively. PLA/GeH nanocomposites containing 0.5 to 2 wt% GeH showed particularly strong antiradical activity against ABTS$^{\bullet+}$. GeH is known as a semiconductor material with high electron mobility,[31,62] which likely facilitates electron transfer, leading to the reduction of the free radicals (DPPH$^{\bullet}$ and ABTS$^{\bullet+}$). This study is the first to report the antioxidant activity of GeH.

The antibacterial activity of the PLA/GeH nanocomposite films was tested against *E. coli* and *C. glutamicum*, representing Gram-negative and Gram-positive strains, respectively. As shown in Fig. 7(c), neat PLA exhibited only slight antibacterial activity against both strains. Germanane is known to possess antibacterial properties against both Gram-positive and Gram-negative bacteria.[18] Consequently, the PLA/GeH nanocomposites were evaluated for GeH-loading-dependent antibacterial activity. The results show that the antibacterial effect increased with GeH content, with the highest activity observed at 5 wt% GeH (71.3% against *E. coli* and 64.8% against *C. glutamicum*). Interestingly, the nanocomposites exhibited slightly stronger antibacterial activity against the Gram-negative strain than the Gram-positive one. The observed antibacterial action is likely

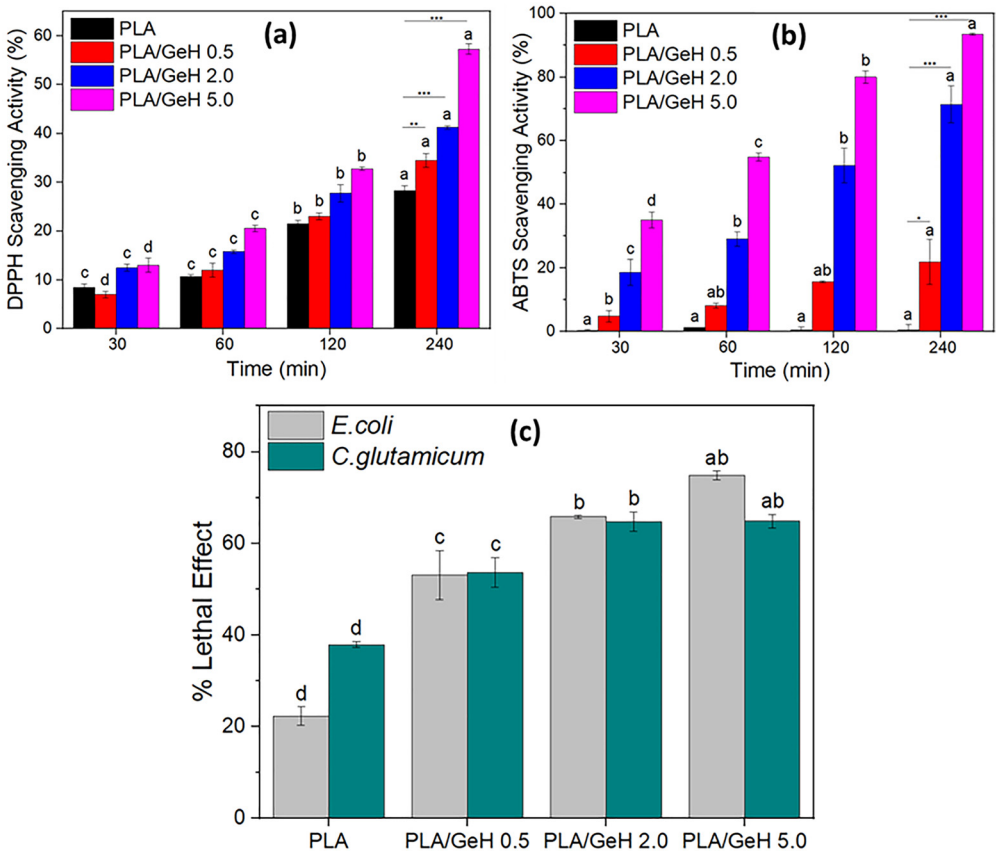

Fig. 7 DPPH (a); and ABTS (b) scavenging activity of neat PLA and PLA/GeH nanocomposite films. Results and error bars correspond to the average and standard deviation of measurements performed on three different specimens (n = 3). (c) Lethal effect of neat PLA and PLA/GeH nanocomposite films against Gram-negative *E. coli* and Gram-positive *C. glutamicum* bacteria. The columns represent the percentages of cell death after 18 h interaction. Results and error bars correspond to the average and standard deviation of measurements performed on at least two different specimens (n = 2). Different lowercase letters or asterisks indicate differences in significance using Tukey's ($p \leq 0.05$) or Dunnett's multiple comparison test (** $p < 0.01$, *** $p < 0.001$), respectively.

due to cell membrane damage caused by germanane, as previously reported.[18] The ''sharp'' edges of the nanosheets at the surface of the nanocomposite cut through the adsorbed bacterium's cell membrane, causing the intracellular matrix to leak, which eventually leads to the bacterium's death.

4. Conclusions

PLA nanocomposites incorporating germanane, a novel 2D nanomaterial, were successfully fabricated *via* solution mixing to investigate the relationship between structure, crystallization behavior, and functional performance. The addition of GeH slightly reduced the thermal stability of PLA, but the nanoplatelets acted as highly effective nucleation agents, significantly accelerating crystallization even at low filler loadings. The presence of GeH also enhanced the nanomechanical performance of the composites, with the optimal effect observed at 0.5 wt%. In addition to mechanical reinforcement, the incorporation of germanane imparted antibacterial and antioxidant functionalities, thereby broadening the application prospects of PLA nanocomposites for advanced food packaging and biomedical technologies.

Author contributions

Theodosis Giousis: investigation, formal analysis, validation, writing – original draft, writing – review & editing; Zoi Terzopoulou: investigation, formal analysis, validation, writing – original draft, writing – review & editing; Maria-Eirini Grigora: investigation, formal analysis, validation; Dimitrios Moschovas and Apostolos Avgeropoulos: investigation, formal analysis; Renia Fotiadou, Stamatia Spyrou and Haralambos Stamatis: investigation, validation, formal analysis, writing – original draft; George Z. Papageorgiou: investigation, formal analysis; Dimitrios Tzetzis: investigation, formal analysis; Dimitrios P. Gournis: conceptualization, validation, supervision; writing – review & editing; Dimitrios N. Bikiaris: conceptualization, validation, supervision, writing – review & editing; Petra Rudolf: validation; supervision; writing – review & editing.

Conflicts of interest

The authors declare no competing financial interest. The authors used OpenAI's ChatGPT (GPT-5, 2025 version) to assist in generating the table of contents in this work. The AI tool was used under OpenAI's commercially licensed terms. All content was reviewed, edited, and verified by the authors for accuracy.

Data availability

The authors declare that all the relevant data supporting the findings of this study are available within the article and its SI. Source data can be provided upon reasonable request. See DOI: **https://doi.org/10.1039/d5ma00676g**.

Acknowledgements

This work received financial support from the Advanced Materials programme of the Zernike National Research Centre under the Bonus Incentive Scheme (BIS) of the Netherlands Ministry of Education, Science, and Culture. The authors thank Iouliana Chrysafi, Laboratory of Advanced Materials and Devices, Department of Physics, Aristotle University of Thessaloniki for performing the TGA measurements. The publication of the article in OA mode was financially supported by HEAL-Link.

References

1 J.-M. Raquez, Y. Habibi, M. Murariu and P. Dubois, Polylactide (PLA)-based nanocomposites, *Prog. Polym. Sci.*, 2013, **38**, 1504–1542, DOI: **10.1016/j.progpolymsci.2013.05.014**.
2 E. Balla, *et al.*, Poly(lactic Acid): a versatile biobased polymer for the future with multifunctional properties—from monomer synthesis, polymerization techniques and molecular weight increase to PLA applications, *Polymers*, 2021, **13**, 1822, DOI: **10.3390/polym13111822**.
3 Z. Terzopoulou, *et al.*, A Decade of Innovation: Synthesis, Properties and Applications of PLA Copolymers, *Prog. Polym. Sci.*, 1991, **167**, 10, DOI: **10.1016/j.progpolymsci.2025.101991**.
4 Z. Liu, *et al.*, A critical review of fused deposition modeling 3D printing technology in manufacturing polylactic acid parts, *Int. J. Adv. Des. Manuf. Technol.*, 2019, **102**, 2877–2889, DOI: **10.1007/s00170-019-03332-x**.
5 D. Notta-Cuvier, *et al.*, Tailoring polylactide (PLA) properties for automotive applications: effect of addition of designed additives on main mechanical properties, *Polym. Test.*, 2014, **36**, 1–9, DOI: **10.1016/j.polymertesting.2014.03.007**.
6 G. Mattana, D. Briand, A. Marette, A. Vásquez Quintero and N. F. de Rooij, Polylactic acid as a biodegradable material for all-solution-processed organic electronic devices, *Org. Electron.*, 2015, **17**, 77–86, DOI: **10.1016/j.orgel.2014.11.010**.
7 O. M. Sanusi, A. Benelfellah, D. N. Bikiaris and N. Aït Hocine, Effect of rigid nanoparticles and preparation techniques on the performances of poly(lactic acid) nanocomposites: a review, *Polym. Adv. Technol.*, 2021, **32**, 444–460, DOI: **10.1002/pat.5104**.
8 R. Banerjee and S. S. Ray, An overview of the recent advances in polylactide-based sustainable nanocomposites, *Polym. Eng. Sci.*, 2021, **61**, 617–649, DOI: **10.1002/pen.25623**.
9 Z. Terzopoulou, *et al.*, Interfacial interactions, crystallization and molecular mobility in nanocomposites of poly(lactic acid) filled with new hybrid inclusions based on graphene oxide and silica nanoparticles, *Polymer*, 2019, **166**, 1–12, DOI: **10.1016/j.polymer.2019.01.041**.
10 G. Z. Papageorgiou, D. S. Achilias, S. Nanaki, T. Beslikas and D. Bikiaris, PLA nanocomposites: effect of filler type on non-isothermal crystallization, *Thermochim. Acta*, 2010, **511**, 129–139, DOI: **10.1016/j.tca.2010.08.004**.
11 H. Balakrishnan, A. Hassan, M. Imran and M. U. Wahit, Toughening of Polylactic Acid Nanocomposites: A Short

Review, *Polym.-Plast. Technol. Eng.*, 2012, **51**, 175–192, DOI: 10.1080/03602559.2011.618329.
12 C. Gonçalves, I. C. Gonçalves, F. D. Magalhães and A. M. Pinto, Poly(lactic acid) composites containing carbon-based nanomaterials: a review, *Polymers*, 2017, **9**, 269, DOI: 10.3390/polym9070269.
13 N. Rohaizad, C. C. Mayorga-Martinez, M. Fojtů, N. M. Latiff and M. Pumera, Two-dimensional materials in biomedical, biosensing and sensing applications, *Chem. Soc. Rev.*, 2021, **50**, 619–657, DOI: 10.1039/D0CS00150C.
14 N. Liu, G. Bo, Y. Liu, X. Xu, Y. Du and S. X. Dou, Recent Progress on Germanene and Functionalized Germanene: Preparation, Characterizations, Applications, and Challenges, *Small*, 2019, **15**, 1805147, DOI: 10.1002/smll.201805147.
15 G. Vogg, M. S. Brandt and M. Stutzmann, Polygermyne – A prototype system for layered Germanium Polymers, *Adv. Mater.*, 2000, **12**, 1278–1281, DOI: 10.1002/1521-4095(200009)12:17<1278::AID-ADMA1278>3.0.CO;2-Y.
16 E. Bianco, *et al.*, Stability and exfoliation of germanane: a germanium graphane analogue, *ACS Nano*, 2013, **7**, 4414–4421, DOI: 10.1021/nn4009406.
17 T. Giousis, *et al.*, Synthesis of 2D germanane (GeH): a new, fast, and facile approach, *Angew. Chem., Int. Ed.*, 2021, **60**, 360–365, DOI: 10.1002/anie.202010404.
18 A. Kouloumpis, *et al.*, Germanane monolayer films as antibacterial coatings, *ACS Appl. Nano Mater.*, 2021, **4**, 2333–2338, DOI: 10.1021/acsanm.0c03149.
19 H. Samsudin, *et al.*, Migration of antioxidants from polylactic acid films: a parameter estimation approach and an overview of the current mass transfer models, *Food Res. Int.*, 2018, **103**, 515–528, DOI: 10.1016/j.foodres.2017.09.021.
20 M. Jamshidian, E. A. Tehrany and S. Desobry, Antioxidants release from solvent-cast PLA film: investigation of PLA antioxidant-active packaging, *Food Bioprocess Technol.*, 2013, **6**, 1450–1463, DOI: 10.1007/s11947-012-0830-9.
21 M. Cvek, *et al.*, Biodegradable films of PLA/PPC and curcumin as packaging materials and smart indicators of food spoilage, *ACS Appl. Mater. nterfaces*, 2022, **14**, 14654–14667, DOI: 10.1021/acsami.2c02181.
22 N. Janani, E. N. Zare, F. Salimi and P. Makvandi, Antibacterial tragacanth gum-based nanocomposite films carrying ascorbic acid antioxidant for bioactive food packaging, *Carbohydr. Polym.*, 2020, **247**, 116678, DOI: 10.1016/j.carbpol.2020.116678.
23 R. Watanabe, *et al.*, Polypropylene-based nanocomposite with enhanced aging stability by surface grafting of silica nanofillers with a silane coupling agent containing an antioxidant, *ACS Omega*, 2020, **5**, 12431–12439, DOI: 10.1021/acsomega.0c01198.
24 H. Shokrani, *et al.*, Green polymer nanocomposites for skin tissue engineering, *ACS Appl. Bio Mater.*, 2022, **5**, 2107–2121, DOI: 10.1021/acsabm.2c00313.
25 A. Mohan, *et al.*, Polyhydroxybutyrate-based nanocomposites for bone tissue engineering, *Pharmaceuticals*, 2021, **14**, 1163, DOI: 10.3390/ph14111163.
26 A. M. Díez-Pascual and J. A. Luceño-Sánchez, Antibacterial activity of polymer nanocomposites incorporating graphene and its derivatives: a state of art, *Polymers*, 2021, **13**, 2105, DOI: 10.3390/polym13132105.
27 L. Tamayo, M. Azócar, M. Kogan, A. Riveros and M. Páez, Copper-polymer nanocomposites: an excellent and cost-effective biocide for use on antibacterial surfaces, *Mater. Sci. Eng., C*, 2016, **69**, 1391–1409, DOI: 10.1016/j.msec.2016.08.041.
28 C. Feng, *et al.*, Germanene-based theranostic materials for surgical adjuvant treatment: inhibiting tumor recurrence and wound infection, *Matter*, 2020, **3**, 127–144, DOI: 10.1016/j.matt.2020.04.022.
29 G. Mansour and D. Tzetzis, Nanomechanical characterization of hybrid multiwall carbon nanotube and fumed silica epoxy nanocomposites, *Polym.-Plast. Technol. Eng.*, 2013, **52**, 1054–1062, DOI: 10.1080/03602559.2013.769581.
30 D. Tzetzis, G. Mansour, I. Tsiafis and E. Pavlidou, Nanoindentation measurements of fumed silica epoxy reinforced nanocomposites, *J. Reinf. Plast. Compos.*, 2013, **32**, 160–173, DOI: 10.1177/0731684412463978.
31 G. Mansour, D. Tzetzis and K. D. Bouzakis, A nanomechanical approach on the measurement of the elastic properties of epoxy reinforced carbon nanotube nanocomposites, *Tribol. Ind.*, 2013, **35**, 190–199.
32 M. S. Blois, Antioxidant Determinations by the Use of a Stable Free Radical, *Nature*, 1958, **181**, 1199–1200, DOI: 10.1038/1811199a0.
33 I. Giotopoulou, R. Fotiadou, H. Stamatis and N.-M. Barkoula, Development of Low-Density Polyethylene Films Coated with Phenolic Substances for Prolonged Bioactivity, *Polymers*, 2023, **15**(23), 4580, DOI: 10.3390/polym15234580.
34 P. E. Athanasiou, M. Patila and R. Fotiadou, *et al.*, Valorization of Wine Lees: Assessment of Antioxidant, Antimicrobial and Enzyme Inhibitory Activity of Wine Lees Extract and Incorporation in Chitosan Films, *Waste Biomass Valorization*, 2024, **15**, 5657–5672, DOI: 10.1007/s12649-024-02524-1.
35 T. Paragkumar N, D. Edith and J.-L. Six, Surface characteristics of PLA and PLGA films, *Appl. Surf. Sci.*, 2006, **253**, 2758–2764, DOI: 10.1016/j.apsusc.2006.05.047.
36 H. Wang and Z. Qiu, Crystallization behaviors of biodegradable poly(L-lactic acid)/graphene oxide nanocomposites from the amorphous state, *Thermochim. Acta*, 2011, **526**, 229–236, DOI: 10.1016/j.tca.2011.10.006.
37 Y.-Q. Zhao, *et al.*, Nanodiamond/poly(lactic acid) nanocomposites: effect of nanodiamond on structure and properties of poly(lactic acid)., *Composites, Part B*, 2010, **41**, 646–653, DOI: 10.1016/j.compositesb.2010.09.003.
38 K. Chrissafis and D. Bikiaris, Can nanoparticles really enhance thermal stability of polymers? Part I: an overview on thermal decomposition of addition polymers, *Thermochim. Acta*, 2011, **523**, 1–24, DOI: 10.1016/j.tca.2011.06.010.
39 A. S. Herc, *et al.*, Crystallization, structure and properties of polylactide/ladder poly(silsesquioxane) blends, *Polymer*, 2020, **201**, 122563, DOI: 10.1016/j.polymer.2020.122563.
40 S. Saeidlou, M. A. Huneault, H. Li and C. B. Park, Poly(lactic acid) crystallization, *Prog. Polym. Sci.*, 2012, **37**, 1657–1677, DOI: 10.1016/j.progpolymsci.2012.07.005.

41 R. Pantani, F. De Santis, A. Sorrentino, F. De Maio and G. Titomanlio, Crystallization kinetics of virgin and processed poly(lactic acid), *Polym. Degrad. Stab.*, 2010, **95**, 1148–1159, DOI: 10.1016/j.polymdegradstab.2010.04.018.
42 R. Androsch, C. Schick and M. L. Di Lorenzo, in *Synthesis, Structure and Properties of Poly(lactic acid)*, ed. M. Laura Di Lorenzo and R. Androsch, Springer International Publishing, 2018, pp. 235–272, DOI: 10.1007/978-3-319-64230-7.
43 Z. Refaa, M. Boutaous and D. A. Siginer, PLA crystallization kinetics and morphology development, *Int. Polym. Process.*, 2018, **33**, 336–344, DOI: 10.3139/217.3525.
44 G. Z. Papageorgiou, *et al.*, Evaluation of the formed interface in biodegradable poly(L-lactic acid)/graphene oxide nanocomposites and the effect of nanofillers on mechanical and thermal properties, *Thermochim. Acta*, 2014, **597**, 48–57, DOI: 10.1016/j.tca.2014.10.007.
45 L. Papadopoulos, *et al.*, Comparative study of crystallization, semicrystalline morphology, and molecular mobility in nanocomposites based on polylactide and various inclusions at low filler loadings, *Polymer*, 2021, **217**, 123457, DOI: 10.1016/j.polymer.2021.123457.
46 K. P. Črešnar, *et al.*, Effects of Ag, ZnO and TiO_2 nanoparticles at low contents on the crystallization, semicrystalline morphology, interfacial phenomena and segmental dynamics of PLA, *Mater. Today Commun.*, 2021, **27**, 102192, DOI: 10.1016/j.mtcomm.2021.102192.
47 E. Tarani, *et al.*, Cold crystallization kinetics and thermal degradation of PLA composites with metal oxide nanofillers, *Appl. Sci.*, 2021, **11**, 3004, DOI: 10.3390/app11073004,.
48 C. Liu, S. Ye and J. Feng, Promoting the dispersion of graphene and crystallization of poly(lactic acid) with a freezing-dried graphene/PEG masterbatch, *Compos. Sci. Technol.*, 2017, **144**, 215–222, DOI: 10.1016/j.compscitech.2017.03.031.
49 R. M. Michell and A. J. Müller, Confined crystallization of polymeric materials, *Prog. Polym. Sci.*, 2016, **54–55**, 183–213, DOI: 10.1016/j.progpolymsci.2015.10.007.
50 M. Avrami, Kinetics of phase change. II Transformation-time relations for random distribution of nuclei, *J. Chem. Phys.*, 1940, **8**, 212–224, DOI: 10.1063/1.1750631.
51 M. Avrami, Granulation, phase change, and microstructure kinetics of phase change. III, *J. Chem. Phys.*, 1941, **9**, 177–184, DOI: 10.1063/1.1750872.
52 M. Avrami, Kinetics of phase change. I General theory, *J. Chem. Phys.*, 1939, **7**, 1103–1112, DOI: 10.1063/1.1750380.
53 A. Maffezzoli, J. Kenny and L. Torre, On the physical dimensions of the Avrami constant, *Thermochim. Acta*, 1995, **269–270**, 185–190, DOI: 10.1016/0040-6031(95)02368-2.
54 A. T. Lorenzo, M. L. Arnal, J. Albuerne and A. J. Müller, DSC isothermal polymer crystallization kinetics measurements and the use of the Avrami equation to fit the data: guidelines to avoid common problems, *Polym. Test.*, 2007, **26**, 222–231, DOI: 10.1016/j.polymertesting.2006.10.005.
55 R. M. D'Ambrosio, *et al.*, Crystallization and stereocomplexation of PLA-mb-PBS multi-block copolymers, *Polymers*, 2018, **10**, 8, DOI: 10.3390/polym10010008.
56 M. Nofar, W. Zhu, C. B. Park and J. Randall, Crystallization kinetics of linear and long-chain-branched polylactide, *Ind. Eng. Chem. Res.*, 2011, **50**, 13789–13798, DOI: 10.1021/ie2011966.
57 V. Krikorian and D. J. Pochan, Unusual crystallization behavior of organoclay reinforced poly(L-lactic acid) nanocomposites, *Macromolecules*, 2004, **37**, 6480–6491, DOI: 10.1021/ma049283w.
58 G. Z. Papageorgiou, *et al.*, Biodegradable poly(ethylene succinate) nanocomposites. Effect of filler type on thermal behaviour and crystallization kinetics, *Polymer*, 2013, **54**, 4604–4616, DOI: 10.1016/j.polymer.2013.06.005.
59 Z. Terzopoulou, D. G. Papageorgiou, G. Z. Papageorgiou and D. N. Bikiaris, Effect of surface functionalization of halloysite nanotubes on synthesis and thermal properties of poly(ε-caprolactone), *J. Mater. Sci.*, 2018, **53**, 6519–6541, DOI: 10.1007/s10853-018-1993-1.
60 L. Papadopoulos, *et al.*, Synthesis and characterization of novel polymer/clay nanocomposites based on poly(butylene 2,5-furan dicarboxylate), *Appl. Clay Sci.*, 2020, **190**, 105588, DOI: 10.1016/j.clay.2020.105588.
61 E. Tarani, *et al.*, Insights into crystallization and melting of high-density polyethylene/graphene nanocomposites studied by fast scanning calorimetry, *Polym. Test.*, 2018, **67**, 349–358, DOI: 10.1016/j.polymertesting.2018.03.029.
62 L. Xu, *et al.*, Performance limits exploration of sub-5 nm monolayer germanane transistors: a first-principle quantum transport simulation, *J. Appl. Phys.*, 2024, **135**(13), 134303, DOI: 10.1063/5.0192389.